RESEARCH ARTICLE | MAY 30 2024

High-temperature insulating ferromagnetic state in chargedisproportionated and spin-state-disproportionated strained SrCoO₂₅ thin film

Sourav Chowdhury ⁽¹⁾; Anupam Jana; Ritu Rawat ⁽¹⁾; Priyanka Yadav ⁽¹⁾; Rajibul Islam ⁽¹⁾; Fei Xue ⁽¹⁾; A. K. Mandal ⁽¹⁾; Sumit Sarkar ⁽¹⁾; Rajan Mishra ⁽¹⁾; R. Venkatesh ⁽¹⁾; D. M. Phase ⁽¹⁾; R. J. Choudhary [■]



APL Mater. 12, 051129 (2024) https://doi.org/10.1063/5.0188767





Articles You May Be Interested In

Direct neutron-diffraction-based measurement of magnetic order in brownmillerite $SrCoO_{2.5}$ and $La_{0.5}Sr_{0.5}CoO_{2.5}$ thin films

APL Mater. (April 2024)

Strain dependent spin-blockade effect realization in the charge-disproportionated ${\rm SrCoO}_{2.5}$ thin films

Appl. Phys. Lett. (July 2021)

A large enhancement of ionic conductivity in $SrCoO_{2.5}$ controlled by isostructural phase transition and negative linear compressibility

Appl. Phys. Lett. (July 2021)





High-temperature insulating ferromagnetic state in charge-disproportionated and spin-state-disproportionated strained SrCoO_{2.5} thin film

Cite as: APL Mater. 12, 051129 (2024); doi: 10.1063/5.0188767 Submitted: 23 November 2023 • Accepted: 9 May 2024 • Published Online: 30 May 2024







Sourav Chowdhury,^{1,2} D Anupam Jana,^{1,3} Ritu Rawat,^{1,4} D Priyanka Yadav,¹ Rajibul Islam,⁵ Fei Xue,⁵ A. K. Mandal,^{1,6} Sumit Sarkar,¹ Rajan Mishra,¹ R. Venkatesh,¹ D. M. Phase,¹ And R. J. Choudhary^{1,3}

AFFILIATIONS

- ¹ UGC-DAE Consortium for Scientific Research, University Campus, Khandwa Road, Indore, Madhya Pradesh 452001, India
- ²Deutsches Elektronen-Synchrotron DESY, Notkestrabe 85, 22607 Hamburg, Germany
- ³CNR-IOM, TASC Laboratory in Area Science Park, 34139 Trieste, Italy and International Centre for Theoretical Physics (ICTP), I-34151 Trieste, Italy
- Department of Mathematics and Physics "Ennio de Giorgi" University of Salento, Via Per Arnesano, 72100 Lecce, Italy
- Department of Physics, University of Alabama at Birmingham, Birmingham, Alabama 35294, USA
- ⁶Indian Institute of Science, CV Raman Rd, Bengaluru, Karnataka 560012, India

ABSTRACT

Ferromagnetic insulators (FMIs) have widespread applications in microwave devices, magnetic tunneling junctions, and dissipationless electronic and quantum-spintronic devices. However, the sparsity of the available high-temperature FMIs has led to the quest for a robust and controllable insulating ferromagnetic state. Here, we present compelling evidence of modulation of the magnetic ground state in a $SrCoO_{2.5}$ (SCO) thin film via strain engineering. The SCO system is an antiferromagnetic insulator with a Neel temperature, T_N , of ~550 K. Applying in-plane compressive strain, the SCO thin film reveals an insulating ferromagnetic state with an extraordinarily high Curie temperature, T_C , of ~750 K. The emerged ferromagnetic state is associated with charge-disproportionation (CD) and spin-state-disproportionation (SSD), involving high-spin Co^{2+} and low-spin Co^{4+} ions. The density functional theory calculation also produces an insulating ferromagnetic state in the strained SCO system, consistent with the CD and SSD, which is associated with the structural ordering in the system. Transpiring the insulating ferromagnetic state through modulating the electronic correlation parameters via strain engineering in the SCO thin film will have a significant impact in large areas of modern electronic and spintronic applications.

© 2024 Author(s). All article content, except where otherwise noted, is licensed under a Creative Commons Attribution (CC BY) license (https://creativecommons.org/licenses/by/4.0/). https://doi.org/10.1063/5.0188767

Ferromagnetic insulators (FMIs) are of significant interest to the materials science community owing to their wide-range applications in various modern technologies, such as permanent magnets, microwave devices. In contrast to the ferromagnetic metals, the FMIs do not suffer from Eddy current losses, which is the key to their low magnetic damping; hence, FMIs are significant for spin-wave-based logics. These are also used as spin-filtering tunneling

barriers in the tunneling magnetoresistance devices. ^{4,5} However, FMIs are rare as the ferromagnetism usually goes hand in hand with the metallic conductivity in the 3*d* transition metal oxides (TMOs), and therefore, the quest for new FMIs with functionality at room temperature remains a vital topic. Along this line, the double perovskite oxides, A₂BB'O₆, where A is alkaline-earth or rare-earth element and B (and B') are transition-metal elements,

a) Author to whom correspondence should be addressed: ram@csr.res.in

show insulating ferromagnetic states with very high Curie temperature (T_C) values, e.g., $Sr_2Fe_{1+x}Re_{1-x}O_6$ ($T_C = 400 \text{ K}$), Sr_2FeMoO_6 $(T_C = 415 \text{ K})$, $^7 \text{Sr}_2\text{CrReO}_6 (T_C = 634 \text{ K})$, $^8 \text{Sr}_2\text{CrOsO}_6 (T_C = 725 \text{ K})$, and Sr₃OsO₆ (T_C = 1060 K), ¹⁰ although many double perovskites show an antiferromagnetic or a spin-glass behavior as well.¹¹ In such oxides, the magnetism is attributed to arise due to the B-site cation ordering; however, their magnetism is mostly affected by the antisite disorder at B/B' sites. In this respect, the brownmillerite (BM) Sr₂Co₂O₅, in short SrCoO_{2,5} (SCO), is quite interesting as it falls in between the perovskite and double perovskite structures. It has a one-dimensional oxygen vacancy channel because of alternate stacking of octahedral (O_h) and tetrahedral (T_d) units along the [001] direction. 12-15 It is categorized as a charge-transfer insulator and is antiferromagnetic with a Neel temperature, T_N ~570 K.¹⁶ Recently, it has been observed that the in-plane compressive strain causes a drastic modification in the electronic ground state of the SCO thin film, which placed this system in the insulating negative chargetransfer energy (Δ) regime inducing ferromagnetic ordering.^{17,18} In this regard, a detailed investigation of the electronic comprehension of the magnetic properties is much needed to better understand the SCO system. A theoretical modeling of the electronic and magnetic ground states is indispensable to showcase the physical property modification with strain in the SCO system. This will improve its functionality toward practical device applications.

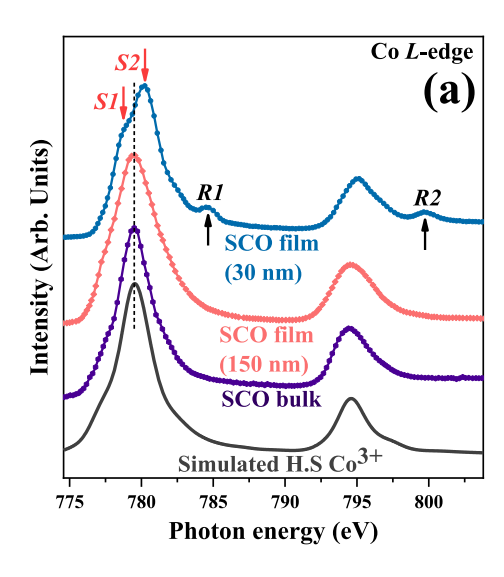
In this article, we have investigated the strain-induced modification in the electronic and magnetic properties of the SCO thin film. The unstrained SCO film shows an antiferromagnetic nature with $T_{\rm N}\sim550$ K, like its bulk counterpart. However, the strained SCO film reveals ferromagnetic ordering with a remarkably high $T_{\rm C}\sim750$ K. The induced ferromagnetic state is associated with the charge-disproportionation (CD) and spin-state-disproportionation (SSD), involving high-spin (H.S) Co^{2+} and low-spin (L.S) Co^{4+} ions. The density functional theory (DFT) calculation also depicts ferromagnetic ordering by inducing strain in the system. The different degrees of structural ordering among the films produce the sharply contrasted electronic and magnetic properties of the strained vs relaxed SCO thin films, as realized from experiment as well as from theory.

Epitaxial SCO films of thicknesses 30 and 150 nm were grown on SrTiO₃ (STO) (001) substrates by pulsed laser deposition (PLD) using a KrF excimer laser (Coherent, USA), $\lambda = 248$ nm, pulse width 20 ns, assisted by the in situ reflection high energy electron diffraction (RHEED) (Staib Instruments, USA). A well-sintered dense pallet of SrCoO_{2.5}, prepared using a solid state reaction route, was used as a target for thin film deposition. The deposition parameters are as follows: substrate temperature 750 °C, oxygen partial pressure during the deposition 100 mTorr, laser fluence at the target 2 J/cm², and target-to-substrate distance 5 cm. After deposition, the thin films were cooled at the same 100 mTorr of O₂ partial pressure. The surface topography of the thin films was studied using an atomic force microscope (AFM) [Nanoscope E AFM from DI, USA (RV)]. The energy dispersive x-ray (EDX) compositional analysis of the thin films was performed with an FE-SEM NOVA Nano SEM-450 by FEI. The x-ray absorption spectroscopy (XAS), x-ray linear dichroism (XLD), and x-ray magnetic circular dichroism (XMCD) studies across the Co $L_{3,2}$ -edge were carried out at room temperature (300 K) in the total electron yield (TEY) mode at the beamline BL-01, Indus-2 at RRCAT, Indore, India. The estimated energy resolution of the XAS was \sim 300 meV. The normalization of the XAS/XLD spectra was performed so that the L_3 pre-edge region was set to zero, in addition to the L_2 post-edge region being set to one. The magnetization measurements were performed by using a 7T SQUID-VSM system (Quantum Design, USA).

Electronic structure calculations were performed within the framework of DFT using the projector augmented wave method implemented in the Vienna *Ab initio* Simulation Package (VASP) package. ¹⁹ We used a 650 eV plane wave energy cutoff as exchange–correlation functional, and we used the generalized gradient approximation (GGA) method²⁰ with intra-site Hubbard energy U = 7 eV and Hund's coupling $J_H = 0.15U$ on Co-3*d* electrons. ^{21–23} We have used the experimental structure for our calculations, and the total energy was converged to 10^{-8} eV with a Gaussian-smearing method. We performed the calculations using a $4 \times 8 \times 8$ Γ-cantered k-mesh with 256 k-points in the Brillouin zone.

The structural characterizations involving out-of-plane θ -2 θ x-ray diffraction (XRD), oblique angle θ –2 θ XRD, and XRD rocking curves of the films were presented elsewhere. 17 These data revealed that the 30 nm film is under 0.4% in-plane compressive strain and the 150 nm film is relaxed.¹⁷ In addition, we have also investigated the surface topology of the thin films with atomic force microscopy (AFM) as shown in Fig. S1, which shows similar surface roughness of both the films. The estimated root mean squire (rms) roughness is of the order of 0.5-0.7 nm in both films. Along with this, we also performed energy dispersive x-ray (EDX) compositional analysis of the thin films. We observed an almost similar composition of Sr and Co and only a ~1% difference in oxygen content among the films. Figure 1(a) shows the isotropic (i.e., the angle between the beam polarization and the sample surface is 45°) XAS of the SCO films along with the bulk SCO reference. The Co L-edge spectrum consists of spin-orbit split components L_2 (Co- $2p_{1/2} \rightarrow$ Co-3d) and L_3 $(\text{Co-}2p_{3/2} \rightarrow \text{Co-}3d)$. The spectral shape and the $L_{3,2}$ peak positions of the 150 nm film are like those of the bulk SCO, implying the Co³⁺ charge state of the 150 nm film. However, the spectrum of the 30 nm film shows CD features S1 and S2 corresponding to 3- δ and 3+ δ charge states of Co and negative Δ features R1 and R2, as discussed in the literature, including our studies.

For the theoretical formulation of the CD and its associated spin-states, we have used the charge transfer multiplet for x-ray absorption spectroscopy (CTM4XAS) program²⁶ under the ligand field and the charge transfer multiplet approach. The simulation was done by varying the crystal-field splitting energy 10Dq, chargetransfer energy Δ , d-d Coulomb repulsion energy U_{dd} , core hole potential U_{pd} (~1.2 times of U_{dd}), and O 2p-Co 3d hybridization strength $\sqrt{3}(pd\sigma)$. The hopping integral between the Co-3d and O-2p orbitals was calculated for the various Co-O bond lengths according to Harrison's descriptions.²⁷ The values of 10Dq were tuned to match the experimental spectra. The values of these parameters, which offer the best match with the experimental spectra, are listed in Table I. The simulation pattern obtained for the 150 nm film (and/or bulk SCO) yields an H.S Co³⁺ state [Fig. 1(a)], consistent with the earlier reports.^{28,29} However, the R1 and R2 features in the experimental spectrum of 30 nm film can be generated in the theoretical spectra only by considering the negative values of Δ for H.S Co²⁺ and L.S and intermediate spin (I.S) states of Co⁴⁺ charge states



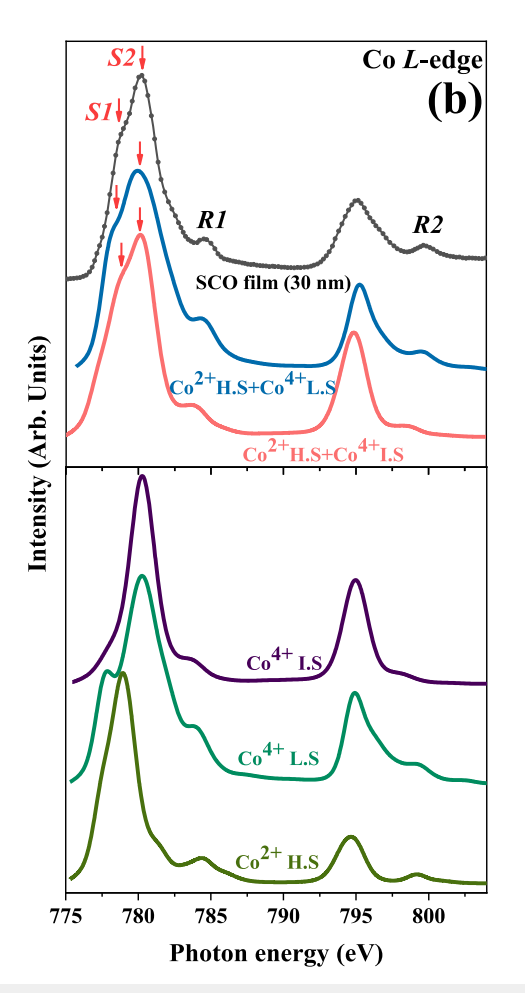


FIG. 1. (a) Co *L*-edge XAS of the 30 and 150 nm SCO films and bulk SCO reference at 300 K along with the simulated spectrum for the H.S Co^{3+} state.^{12,17} The negative Δ features (R1 and R2) and the CD features (S1 and S2) are indicated by the vertical arrows. (b) (Lower panel) Simulated XAS for the Co^{2+} H.S, Co^{4+} L.S, and Co^{4+} I.S states. (Upper panel) Comparison of the Co^{2+} H.S + Co^{4+} L.S and Co^{2+} H.S + Co^{4+} L.S theoretical spectra with the experimental spectrum of the 30 nm SCO film.

[lower panel, Fig. 1(b)]. The upper panel of Fig. 1(b) suggests that the best match with the experimental spectrum occurs when we consider a linear combination of H.S Co²⁺ and L.S Co⁴⁺ simulated spectra. This is a crucial finding since it indicates that in the 30 nm film,

TABLE I. Values of 10Dq, Δ , U_{dd} , U_{pd} , and $\sqrt{3}(pd\sigma)$ parameters were used to simulate the Co *L*-edge spectra for the different charge states.

Charge state (Spin state)		Δ (eV)	U _{dd} (eV)	U _{pd} (eV)	$\sqrt{3(pd\sigma)}$ (eV)
Co ³⁺ (H.S)	1.4	3	6.2	7.3	2.0
Co ²⁺ (H.S)	1.3	-1	4.5	6.3	2.4
Co ⁴⁺ (L.S)	2.1	-8.5	10	14	3.6
Co ⁴⁺ (I.S)	1.7	-5.0	6.5	8	3.2

along with CD, spin-state-ordering or spin-state-disproportionation (SSD), associated with the H.S Co²⁺ and L.S Co⁴⁺ charge states, also occur. Thus, it is inferred that the H.S Co³⁺ state in the relaxed 150 nm film (and/or bulk SCO) is charge as well as spin-state disproportionated into H.S Co²⁺ and L.S Co⁴⁺ states in the strained 30 nm film; $2\text{Co}^{3+}(\text{H.S}) \rightarrow \text{Co}^{2+}(\text{H.S}) + \text{Co}^{4+}(\text{L.S})$.

In the present case of the SCO system (both bulk and thin films), all the cations exist in both the O_h and T_d units. Thus, in our theoretical formulation of Co L-edge XAS through CTM4XAS, apparently, we should consider both the O_h and T_d units. Under the protocol of the simulations, 26 it is observed that whether we consider O_h or T_d symmetry, besides the variations in the overall spectral intensity, all the features remain the same. Thus, although both the O_h and T_d symmetries are present in the SCO system (both bulk and thin film), its L-edge spectra can be simulated considering either of the O_h and T_d symmetries. Therefore, to avoid the complicacy of considering four individual theoretical spectra [two charge

states ($\mathrm{Co^{2^+}}$ and $\mathrm{Co^{4^+}}$) and each with both the O_h and T_d units] to theoretically generate the spectrum and compare it with the experimental spectrum, we only consider O_h units for the XAS simulation. In addition, it is to be noted that the crystal field energy (10Dq) and all the electronic correlation parameters, e.g., Δ , U_{dd} , U_{pd} , and $pd\sigma$, are different depending on whether the metal cations are situated in the O_h or T_d units. As we need to accommodate the structural distortion effect due to the presence of T_d units, we put slightly different values of the electronic correlation parameters as compared to the usual in our simulation to match with the experimental L-edge spectra.

The metal cation with a fixed charge-state can have different peak positions in the L-edge XAS depending on whether it is situated in the O_h or T_d units, as is well-known for the Fe₃O₄ compound, where the Fe³⁺ ions occupy both the O_h and T_d coordination. ^{30,31}

Therefore, it can be assumed that the S1 and S2 features in the experimental Co L-edge spectrum of the 30 nm SCO film arise due to the Co³+ ions occupying the O_h and T_d units and not due to the Co²+ and Co⁴+ charge-disproportionation. However, the S1 and S2 features appear symmetrically on the lower and higher energy sides of the Co³+ charge-state position, respectively [Fig. 1(a)], which indicates that the charge states correspond to the S1 and S2 features are Co²+ and Co⁴+, respectively, and not due to some other multiplets. Moreover, the O_h and T_d units are also present in the 150 nm SCO film as well as in bulk SCO, which do not depict such S1 and S2 features. As the 150 nm SCO film (and/or bulk SCO) does not depict any fine spectre features, it indicates that the spectrum is not a superposition of two spectra. Hence, we preclude the affinity of S1 and S2 features with the O_h and T_d symmetries.

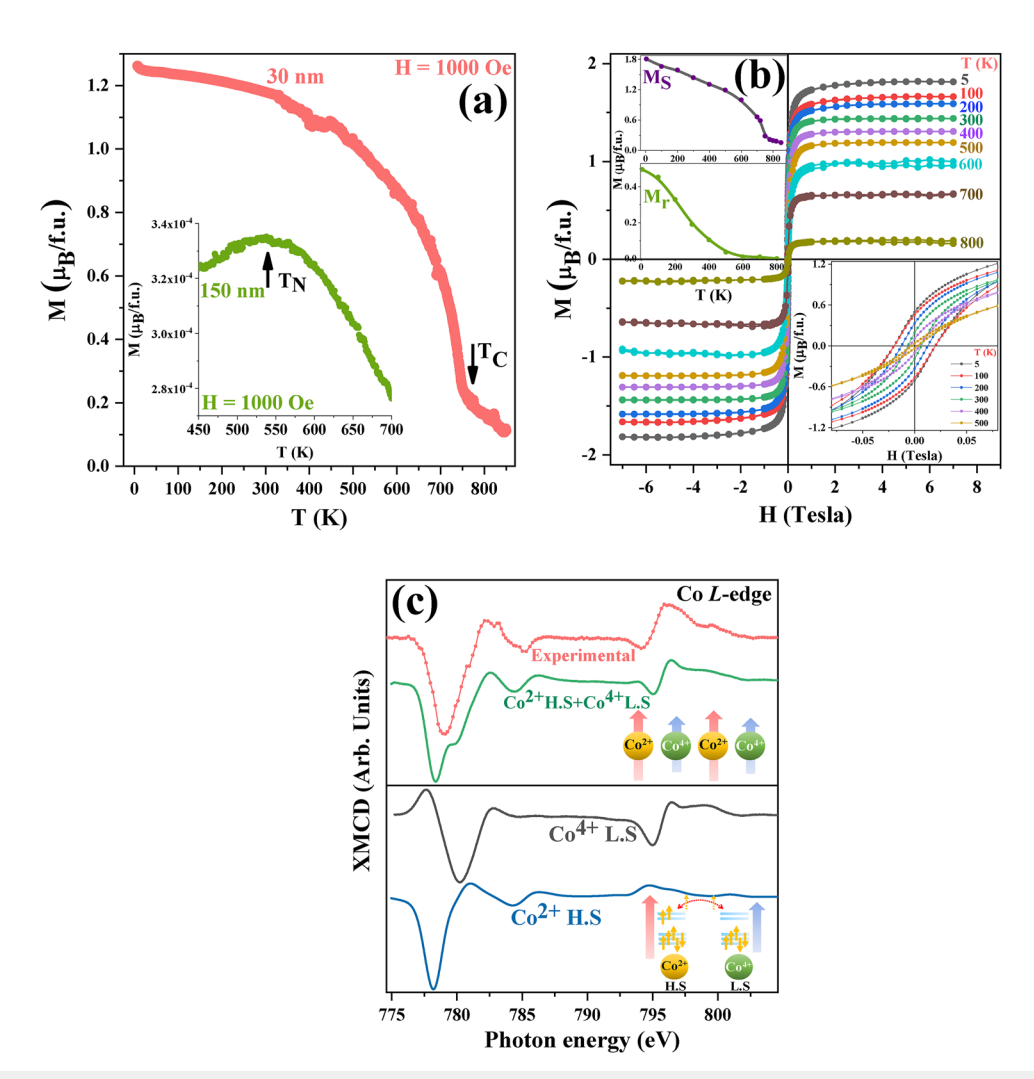


FIG. 2. (a) M–T behavior of (main) 30 nm; inset: 150 nm SCO films. (b) T-dependent M–H hysteresis behavior of the 30 nm SCO film. (Lower inset) Zoomed view of the M–H curves. (Upper inset) T variation of M_s and M_r . (c) (Lower panel) Simulated XMCD spectra for the Co^{2+} H.S and Co^{4+} L.S states. (Upper panel) Comparison of the Co^{2+} H.S + Co^{4+} L.S theoretical spectrum with the experimental XMCD spectrum¹⁷ of the 30 nm SCO film. The insets show Co^{2+} and Co^{4+} parallel alignments, causing ferromagnetic ordering in the system.

The magnetization measurements are shown in Figs. 2(a) and 2(b). The 150 nm film reveals antiferromagnetic ordering with $T_N \sim 550$ K [inset, Fig. 2(a)], close to that reported for the bulk SCO (T_N = 570 K).¹⁶ Interestingly, the 30 nm film depicts ferromagnetic (or ferrimagnetic) ordering with an exceptionally high $T_C \sim 750 \text{ K}$ [Fig. 2(a)]. The magnetization-field (M-H) hysteresis behavior recorded at different temperatures (T), ranging from 5 to 800 K, is shown in Fig. 2(b). The lower inset of Fig. 2(b) displays the zoomed-in view of the M-H curves, showing the clear hysteresis behaviors. The obtained values of the saturation-magnetization (M_s) and the remanent-magnetization (M_r) from the M-H curves are plotted against T in the upper insets of Fig. 2(b), which shows that M_r decays more rapidly than M_s. The M_r arises because of the anisotropic response of the magnetic moments in the increasing and decreasing field cycles of the M-H measurements. There is a competition between anisotropy energy and thermal energy. In the strained SCO film, at higher temperatures (600 K or above), the thermal energy dominates the anisotropy energy; hence, M_r decreases rather rapidly, although the system still reveals a soft ferromagnetic nature. A similar behavior is also observed in other soft ferromagnets, such as Sr₃OsO₆ thin film, ¹⁰ Fe oxide nanoparticles, ³² and GaMnAs/GaAs superlattices.³³ We also observe a signature of the short-range magnetic correlations from the non-vanishing M_s above T_C. The isoelectronic LaCoO₃ thin film is also known to depict a strain-induced ferromagnetic (or ferrimagnetic) insulating state in an otherwise paramagnetic insulating bulk counterpart.3

At 300 K, the 30 nm film reveals a finite XMCD signal, confirming its ferromagnetic (or ferrimagnetic) nature, whereas the 150 nm film does not show any XMCD signal, consistent with its antiferromagnetic nature. To know the electronic state contribution to the ferromagnetic ordering in the 30 nm film, we have further simulated the Co *L*-edge XMCD spectra for different charge and spin-states of Co [lower panel, Fig. 2(c)], considering the same input parameters as used for the XAS simulations. The Co²⁺H.S + Co⁴⁺L.S combined spectrum shows a good match with the experimental XMCD spectrum [upper panel, Fig. 2(c)], further validating our charge as well as spin-state disproportionation concept. The significance of the above analysis implies the contributions of CD and SSD states in producing the ferromagnetic ordering in the 30 nm SCO thin film.

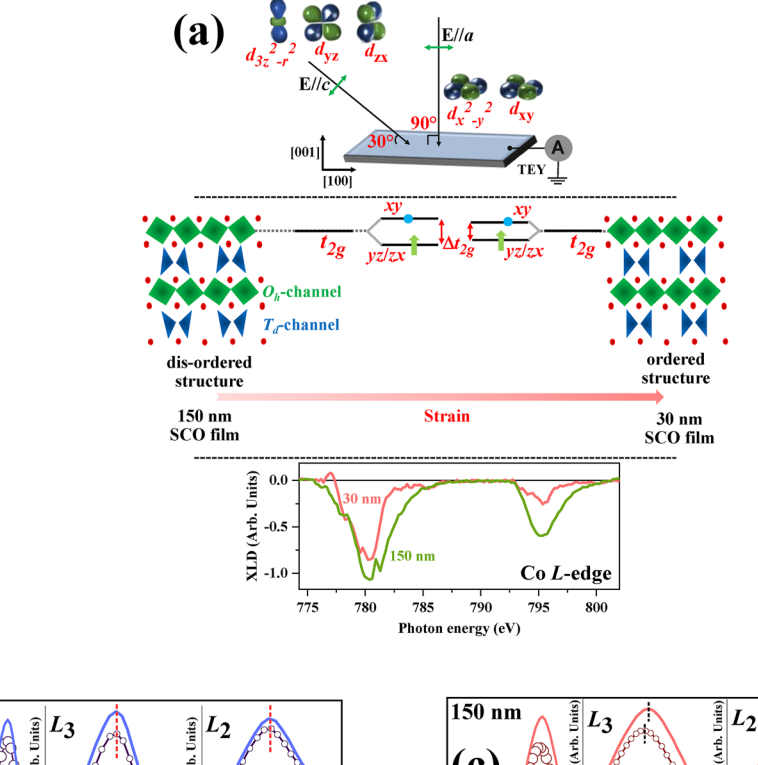
Now, we try to correlate the electronic and magnetic properties of the SCO thin films. The 150 nm film (and/or bulk SCO) is in a Co³⁺ H.S state, which leads to the Co³⁺-O-Co³⁺ super-exchange interaction, producing antiferromagnetic ordering. However, the H.S Co^{2+} (S = 3/2) and L.S Co^{4+} (S = 1/2) disproportionated states in the 30 nm film cannot bring antiferromagnetic ordering because of their unequal effective spins, and therefore, the system should be either ferromagnetic or ferrimagnetic. Furthermore, by summing the theoretical XMCD spectra of Co²⁺ and Co⁴⁺ states, we produce the experimental XMCD spectrum of the 30 nm film, divulging the parallel spin alignment in the system [schematic view, upper inset, Fig. 2(c)] and ruling out the possibility of ferrimagnetic ordering in the system. The ferromagnetic interaction between the H.S Co² and L.S Co⁴⁺ ions can be understood from the lowest energy virtual charge fluctuation between these ions. When virtual charge fluctuation has taken place from the H.S Co²⁺ site, the spin does not need to flip to the L.S Co⁴⁺ site [schematic view, lower inset, Fig. 2(c)], explaining a ferromagnetic interaction in the system.

Figures 3(b) and 3(c) display the polarization-dependent Co Ledge XAS and XLD spectra of the 30 and 150 nm SCO films, respectively. The experimental geometry for the polarization-dependent XAS measurements is schematically shown in the upper panel of Fig. 3(a). It is evident that if the electric field vector of the synchrotron radiation (E) is parallel to the sample surface, the spectrum (I_{ab}) gives the information of the in-plane orbitals $(x^2 - y^2 \text{ and } xy)$. Meanwhile, for E perpendicular to the sample surface, the spectrum (I_c) gives the information of the majority of the out-of-plane orbitals $(3z^2 - r^2, yz, \text{ and } zx)$. The average positive {or negative} XLD signal, defined as (I_c-I_{ab}) , will reveal the in-plane (ab-plane) [or the out-of-plane (c-axis)] orbital polarization. The negative XLD signal is observed in both the SCO films [Figs. 3(b) and 3(c)], which divulges their out-of-plane orbital polarization, indicating relatively higher energy positions of the in-plane orbitals than the out-of-plane orbitals. Therefore, the electrons mostly prefer to occupy the out-ofplane orbitals and the holes are left behind in the in-plane orbitals, causing the out-of-plane orbital polarization in both the SCO films, as schematically shown in the middle panel of Fig. 3(a).

It is interesting to note that the 150 nm film depicts orbital splitting, as can be seen from the difference in I_{ab} and I_c peak positions by ~200 meV in both the $L_{3,2}$ -edges [inset of Fig. 3(c)], which is not the case for the 30 nm film [inset of Fig. 3(b)]. Such an orbital splitting in the polarization-dependent XAS of perovskite TMOs arises due to the disorder in the TMO₆ octahedra, such as octahedral rotation or bending. 36,37 Thus, in the present case, the occurrence of orbital splitting in the 150 nm film and its absence in the 30 nm film indicate that the former possesses a higher degree of CoO₆ O_h and CoO₄ T_d distortions compared to the latter. The obtained results from Figs. 3(b) and 3(c) are schematically illustrated in the middle panel, Fig. 3(a), which divulges that the energy separation between the in-plane and out-of-plane orbitals is larger in the 150 nm film because of its higher degree of structural distortion than the 30 nm film.

The larger energy separation in the 150 nm film causes a higher electron population difference between the in-plane and out-ofplane orbitals, as can be obtained from the stronger XLD signal in the 150 nm film than the 30 nm film, as displayed in the lower panel of Fig. 3(a). In the relaxed 150 nm film, the electronic configurations of H.S Co³⁺ are $t_{2g}^{4}e_{g}^{2}$ and $e_{g}^{3}t_{2g}^{3}$ in the O_{h} and T_{d} symmetries, respectively. Thus, both the t_{2g} orbitals (in O_h symmetry) and e_g orbital (in T_d symmetry) are likely to participate in the XLD signal because of their partial field orbitals. In the strained 30 nm film, considering the O_h symmetry, the H.S Co^{2+} and L.S Co^{4+} have $t_{2g}{}^5e_g{}^2$ and $t_{2g}{}^5e_g{}^0$ configurations, respectively. Considering ering the T_d symmetry, the H.S Co²⁺ and L.S Co⁴⁺ have $e_g^4 t_{2g}^3$ and $e_g^4 t_{2g}^{-1}$ configurations, respectively. Since the e_g state is either halffilled or empty in the O_h symmetry (or completely filled in the T_d symmetry), only the t_{2g} orbital is likely to participate in the XLD signal. Therefore, we have compared the separation between the inplane and out-of-plane components of the t_{2g} orbitals of the films only, as the t_{2g} orbitals participate in the XLD signals in both the 30 and 150 nm films [middle panel of Fig. 3(a)].

In this regard, it is worthwhile to mention that the structural ordering is ascribed to the reason for high $T_{\rm C}$ ferromagnetic ordering in the double perovskites. To For instance, the recently reported ferromagnetic Sr_3OsO_6 thin film reveals the highest $T_{\rm C}$ (~1060 K)



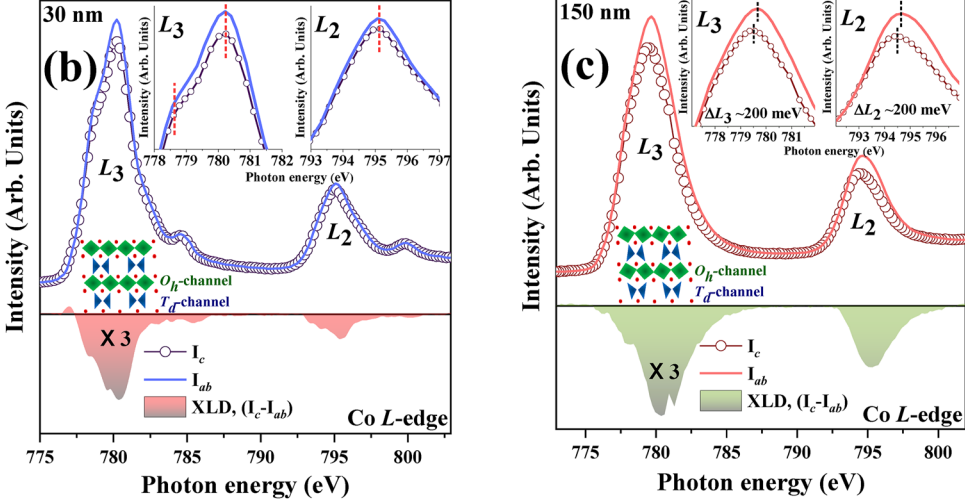


FIG. 3. (a) (Upper panel) Experimental geometry of the polarization-dependent XAS measurements. (Middle panel) Schematic illustration of the orbital polarization and orbital splitting caused by COO_6 O_h and COO_4 T_d distortions and their variation with strain in the SCO films. The electrons and holes are represented by arrows and circles, respectively. The energy separations between the in-plane and out-of-plane orbitals are defined as Δt_{2g} . (Lower panel) Comparison of the XLD signals of the SCO films. The polarization-dependent XAS and XLD signals of the (b) 30 and (c) 150 nm SCO films. The inset shows the comparison of the $L_{3,2}$ peak positions of the I_{ab} and I_c spectra of the films.

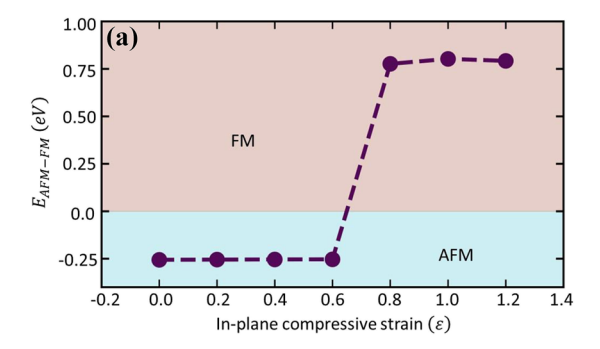
among the TMOs. ¹⁰ However, the isoelectronic Ca₃OsO₆ system is antiferromagnetic with $T_N \sim 50~K$. ³⁸ The difference in their magnetic ground state is attributed to the different crystal structures, where Sr₃OsO₆ is cubic with a high degree of OsO₆ O_h ordering; in contrast, Ca₃OsO₆ is monoclinic with tilted OsO₆ O_h . ^{10,38} In addition, the degree of O_h distortion is also ascribed to be associated with the sharply contrasted magnetic ground states in another pair of

isoelectronic perovskite systems, SrRuO₃ (pseudo-cubic, ferromagnetic metal) and CaRuO₃ (orthorhombic, paramagnetic metal).³⁹ Although the global structures of both the studied SCO films are orthorhombic-BM,¹⁷ the different degrees of structural ordering at the local level could be associated with the sharp dissimilar magnetic properties of the studied strained vs relaxed SCO thin films. Although the different degrees of local structural ordering are visu-

alized qualitatively from the polarization-dependent XAS study, a quantitative understanding of it through high-resolution transmission electron microscopy will provide more insights into the structural ordering, which needs to be further studied.

Using experimental parameters, we have performed DFT calculations on SCO systems. In the absence of strain, our results indicate the antiferromagnetic (AFM) configuration as the ground state. A compressive in-plane stain (ϵ) and tensile out-of-plane stain (ϵ) combine to make the ferromagnetic (FM) configuration the ground state. Figure 4(a) demonstrates the effect of in-plane compressive strain on the difference in energy of two distinct configurations ($E_{\rm AFM-FM}$); the phase transition occurs at in-plane compression $\epsilon \sim 0.7\%$ in our calculation, while the experimentally measured compressive strain is 0.4%.

Figure 4(b) displays the calculated crystal structures in the unstrained AFM and strained FM states of the SCO systems. The crystal structure at the AFM state is more disordered as compared to the same in the FM state, as can be visualized from the horizontal and vertical straight dashed lines in this figure. Both the apical and basal oxygens, shown by the red spheres, are at longer distances from the vertical and horizontal straight dashed lines in the unstrained AFM structure as compared to the strained FM structure. For instance, the Co–O–Co bond angles between the O_h geometries are found to be 174.62° and 177.66° for unstrained and strained cases, respectively. The same between O_h and T_d geometries are



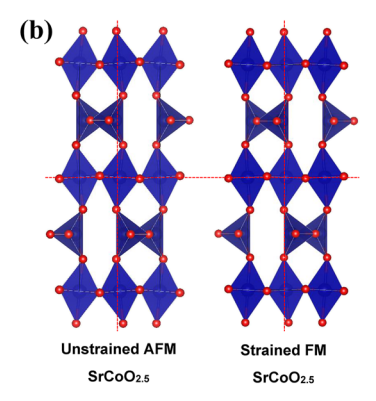


FIG. 4. (a) The change in energy state due to the in-plane compressive strain in the SCO system. (b) Calculated crystal structures for the unstrained SCO (left) and strained SCO (right) systems. The vertical and horizontal straight dashed lines are guides to the eye.

found to be 167.34° and 170.63° for unstrained and strained cases, respectively. This divulges a higher degree of rotation and bending in CoO₆ O_h and CoO₄ T_d units in the unstrained AFM structure than the strained FM structure. This further supports the structural ordering facilitated magnetic ordering in SCO systems, in excellent agreement with our polarization-dependent XAS/XLD analysis.

We have computed the Bader charge difference of cobalt atoms between various O_h and T_d units. The Bader charge difference (e) is determined by calculating the difference in charges between two cobalt atoms that are part of separate O_h and T_d units [charge difference (e) = (site charge of Co1 – site charge of Co2) $O_{Dh/Td}$]. Our DFT calculated Bader charge differences for unstrained and strained SCO films are 0 for both the O_h and T_d units and 0.19e and 0.15e in O_h and T_d units, respectively (Table II), which is in excellent agreement with the presence of CD on alternate Co sites in strained SCO, which is absent in relaxed SCO.

We also observed a difference in the calculated band structure and density of states (DOS) between the strained and unstrained SCO systems, which is presented in the supplementary material (Fig. S2).

The observed ferromagnetic state in the strained SCO film in the present study is markedly different from the study on the same system (SCO/STO) by Jeen *et al.*, where the authors observed an antiferromagnetic state in the strained SCO film, same as the bulk SCO.¹⁴ However, the possibility of the difference in the electronic and magnetic properties in this system was predicted by the same group⁴⁰ based on the different local crystal structures. In addition, the reason for such differences is verbosely addressed elsewhere.¹⁷ It is worthwhile to note that we have investigated the charge and spin states of the films only at 300 K. However, there is a possibility of spin-state transition of Co⁴⁺ from L.S state toward I.S or H.S by increasing temperature, similar to the temperature-driven spin-state transition in LaCoO₃, ^{41–43} which needs to be further studied.

The charge-disproportionation also leads to the bond-disproportionation of short-bond (compressed octahedra) and long-bond (elongated octahedra) in RNiO₃ (R: rare-earth ion), CaFeO₃, and BaBiO₃ systems.^{44–48} The systems accommodate the alternate short and long bond ordering by minimizing the octahedral rotation or bending, i.e., by minimizing structural disorder. For example, the LaNiO₃/LaAlO₃ superlattice on the STO substrate reveals charge-disproportionation and shows lesser structural disorder relative to the non-disproportionated LaNiO₃/LaAlO₃ superlattice on the LaAlO₃ substrate.³⁶ We also observed that the charge-disproportionated 30 nm film has a lesser structural disorder than the non-disproportionated 150 nm film. Thus, it can be stated

TABLE II. DFT calculated Bader charges on Co sites for unstrained and strained SCO systems in both the O_h and T_d units.

	Site charges (e)		
System (Units)	Co1 Co2 C		Charge difference (e)
Unstrained SCO (O_h)	7.43	7.43	0
Unstrained SCO (T_d)	7.55	7.55	0
Strained SCO (O_h)	7.47	7.66	0.19
Strained SCO (T_d)	7.57	7.72	0.15

that the charge-disproportionated state is more likely to form in the structurally ordered state rather than the structurally distorted state. It was also observed that the 30 nm film has a stronger O 2p-Co 3d hybridization strength than the 150 nm film (and/or bulk SCO).¹⁷ The stronger O 2p-Co 3d hybridization is also consistent with the observed higher degree of CoO₆ O_h and CoO₄ T_d ordering in the 30 nm film relative to the 150 nm film since the structural disorder deteriorates the hybridization strength.⁴⁹ Tuning the magnetic ground state by altering the electronic correlation parameters shows a way to modulate the magnetic state via applying an electric field⁵⁰ besides strain engineering, which provides a new route toward energy-efficient spintronics in SCO-based systems.⁵¹ In this line, modification of physical properties by ferroelectric/piezoelectric strain through substrate's lattice parameter modification via electric field enables an engineering method that allows for the creation of tailored states similar to manganite thin films on Pb(Mg_{1/3}Nb_{2/3})O₃-PbTiO₃ substrates.⁵²

In summary, we observed the insulating ferromagnetic state with exceptionally high $T_{\rm C}\sim750$ K in the strained SrCoO $_{2.5}$ thin film in an otherwise antiferromagnetic insulator ($T_{\rm N}\sim550$ K) in its unstrained (and/or bulk) counterpart. The emerged ferromagnetic state is associated with charge-disproportionation and spin-state-disproportionation, involving high-spin Co^{2+} and low-spin Co^{4+} states. Along with the charge-disproportionation and spin-state-disproportionation, local structural ordering in the strained SrCoO $_{2.5}$ film provides the necessary condition of the ferromagnetic state akin to the structural ordering facilitated ferromagnetics min double perovskites, as observed from experiment as well as theory. Inducing such a high temperature sustainable insulating ferromagnetic state in the strained SrCoO $_{2.5}$ thin film makes it a promising candidate for future energy-efficient electronic and quantum-spintronic device applications.

The supplementary material contains atomic force microscopy (AFM) images of the thin films. It also contains strain dependent band structures and density of states (DOS) calculations for the thin films.

The authors thank A. Wadikar and R. Sah for helping with XAS and XMCD measurements. They also thank M. Hoesch, S. Majumder, and S. Pal for the crucial discussions. The authors acknowledge DST-SERB for the grant under the Project No. CRG/2021/001021. R.I. and F.X. acknowledge the support of the National Science Foundation under Grant No. OIA-2229498, through the University of Birmingham Alabama. R.I. and F.X. acknowledge the access to the computing facility Cheaha at the University of Birmingham Alabama.

AUTHOR DECLARATIONS

Conflict of Interest

The authors have no conflicts to disclose.

Author Contributions

Sourav Chowdhury: Conceptualization (equal); Data curation (equal); Formal analysis (equal); Investigation (equal); Methodology

(equal); Software (equal); Supervision (equal); Validation (equal); Visualization (equal); Writing - original draft (equal); Writing review & editing (equal). Anupam Jana: Data curation (equal); Investigation (equal); Validation (equal); Writing - review & editing (equal). Ritu Rawat: Data curation (equal); Investigation (equal); Validation (equal); Writing - review & editing (equal). Priyanka Yadav: Data curation (equal); Methodology (equal); Validation (equal); Writing - review & editing (equal). Rajibul Islam: Data curation (equal); Methodology (equal); Visualization (equal); Writing - review & editing (equal). Fei Xue: Data curation (equal); Investigation (equal); Validation (equal); Writing – review & editing (equal). A. K. Mandal: Data curation (equal); Investigation (equal); Visualization (equal); Writing - review & editing (equal). Sumit Sarkar: Data curation (equal); Formal analysis (equal); Visualization (equal); Writing - review & editing (equal). Rajan Mishra: Data curation (supporting); Formal analysis (supporting); Investigation (supporting). R. Venkatesh: Data curation (supporting); Formal analysis (supporting); Investigation (supporting). D. M. Phase: Conceptualization (lead); Funding acquisition (lead); Project administration (lead); Supervision (lead); Validation (lead); Writing - review & editing (lead). R. J. Choudhary: Conceptualization (lead); Funding acquisition (lead); Project administration (lead); Supervision (lead); Validation (lead); Visualization (lead); Writing – original draft (lead); Writing - review & editing (lead).

DATA AVAILABILITY

The data that support the findings of this study are available from the corresponding author upon reasonable request.

REFERENCES

- ¹P. Tenaud, A. Morel, F. Kools, J. M. Le Breton, and L. Lechevallier, J. Alloys Compd. **370**, 331 (2004).
- ²Y. Naito and K. Suetake, IEEE Trans. Microwave Theory Tech. **19**, 65 (1971).
- ³Y. Kajiwara, K. Harii, S. Takahashi, J. Ohe, K. Uchida, M. Mizuguchi, H. Umezawa, H. Kawai, K. Ando, K. Takanashi, S. Maekawa, and E. Saitoh, Nature 464, 262 (2010).
- ⁴J. S. Moodera, X. Hao, G. A. Gibson, and R. Meservey, Phys. Rev. Lett. **61**, 637 (1988).
- ⁵K. Uchida, J. Xiao, H. Adachi, J. Ohe, S. Takahashi, J. Ieda, T. Ota, Y. Kajiwara, H. Umezawa, H. Kawai, G. E. Bauer, S. Maekawa, and E. Saitoh, Nat. Mater. **9**, 894 (2010).
- ⁶C. Sohn, E. Skoropata, Y. Choi, X. Gao, A. Rastogi, A. Huon, M. A. McGuire, L. Nuckols, Y. Zhang, J. W. Freeland, D. Haskel, and H. N. Lee, Adv. Mater. 31, 1805389 (2019).
- ⁷ K. I. Kobayashi, T. Kimura, H. Sawada, K. Terakura, and Y. Tokura, Nature 395, 677 (1998).
- ⁸H. Kato et al., Appl. Phys. Lett. **81**, 328 (2002).
- ⁹Y. Krockenberger et al., Phys. Rev. B 75, 020404(R) (2007).
- ¹⁰Y. K. Wakabayashi, Y. Krockenberger, N. Tsujimoto, T. Boykin, S. Tsuneyuki, Y. Taniyasu, and H. Yamamoto, Nat. Commun. 10, 535 (2019).
- ¹¹P. D. Battle, T. C. Gibb, A. J. Herod, S. H. Kim, and P. H. Munns, J. Mater. Chem. 5, 865 (1995).
- ¹²S. Chowdhury, R. J. Choudhary, and D. M. Phase, Appl. Phys. Lett. **119**, 021901 (2021).
- ¹³S. Chowdhury, R. J. Choudhary, and D. M. Phase, J. Alloys Compd. **108**, 159296 (2021).
- ¹⁴H. Jeen, W. S. Choi, M. D. Biegalski, C. M. Folkman, I. C. Tung, D. D. Fong, J. W. Freeland, D. Shin, H. Ohta, M. F. Chisholm, and H. N. Lee, Nat. Mater. 12, 1057 (2013).

- ¹⁵S. Chowdhury, A. Jana, A. Mandal, S. Sarkar, R. J. Choudhary, and D. M. Phase, J. Phys. Chem. C **125**(31), 17537–17545 (2021).
- ¹⁶T. Takeda and H. Watanabe, J. Phys. Soc. Jpn. 33, 973 (1972).
- ¹⁷S. Chowdhury, A. Jana, M. Kuila, V. R. Reddy, R. J. Choudhary, and D. M. Phase, ACS Appl. Electron. Mater. 2, 3859 (2020).
- ¹⁸S. Chowdhury, A. Jana, A. Kumar Mandal, R. J. Choudhary, and D. M. Phase, ACS Appl. Electron. Mater. **3**, 3060 (2021).
- ¹⁹G. Kresse and J. Furthmüller, Phys. Rev. B **54**, 11169 (1996).
- ²⁰J. P. Perdew, K. Burke, and M. Ernzerhof, Phys. Rev. Lett. 77, 3865 (1996).
- ²¹K. Wilbert, A.-M. Pradipto, and A. Agung Nugroho, J. Phys.: Conf. Ser. 2243, 012091 (2022).
- ²²R. Islam, S. Mardanya, A. Lau, G. Cuono, T.-R. Chang, B. Singh, C. M. Canali, T. Dietl, and C. Autieri, Phys. Rev. B **107**, 125102 (2023).
- ²³ N. Gonzalez Szwacki, J. A. Majewski, and T. Dietl, Phys. Rev. B 83, 184417 (2011).
- ²⁴F. M. F. de Groot, J. C. Fuggle, B. T. Thole, and G. A. Sawatzky, Phys. Rev. B **42**, 5459 (1990).
- ²⁵ M. Abbate, L. Mogni, F. Prado, and A. Caneiro, Phys. Rev. B **71**, 195113 (2005).
- ²⁶E. Stavitski and F. M. F. de Groot, Micron **41**(7), 687 (2010).
- ²⁷W. A. Harrison, J. Mol. Struct. **71**, 355 (1981); W. H. Freeman, and Co., San Francisco, 1980.
- ²⁸S. Hu, Z. Yue, J. S. Lim, S. J. Callori, J. Bertinshaw, A. Ikeda-Ohno, T. Ohkochi, C.-H. Yang, X. Wang, C. Ulrich, and J. Seidel, Adv. Mater. Interfaces 2, 1500012 (2015).
- ²⁹ J. Lim and J. Yu, Phys. Rev. B **98**, 085106 (2018).
- ³⁰ S. D. Oberdick, A. Abdelgawad, C. Moya, S. Mesbahi-Vasey, D. Kepaptsoglou, V. K. Lazarov, R. F. L. Evans, D. Meilak, E. Skoropata, J. van Lierop, I. Hunt-Isaak, H. Pan, Y. Ijiri, K. L. Krycka, J. A. Borchers, and S. A. Majetich, Sci. Rep. 8, 3425 (2018).
- ³¹ D. M. Phase, G. Panchal, R. Rawat, S. Tiwari, R. Prakash, D. Jain, and R. J. Choudhary, J. Magn. Magn. Mater. 482, 296–300 (2019).
- ³²S. G. Greculeasa, P. Palade, G. Schinteie, A. Leca, F. Dumitrache, I. Lungu, G. Prodan, A. Kuncser, and V. Kuncser, Sci. Rep. 10, 17174 (2020).
- ³³S. J. Chung, S. Lee, I. W. Park, X. Liu, and J. K. Furdyna, J. Appl. Phys. **95**, 7402 (2004)
- ³⁴J. Fujioka, Y. Yamasaki, A. Doi, H. Nakao, R. Kumai, Y. Murakami, M. Nakamura, M. Kawasaki, T. Arima, and Y. Tokura, Phys. Rev. B 92, 195115 (2015).

- ³⁵G. E. Sterbinsky, R. Nanguneri, J. X. Ma, J. Shi, E. Karapetrova, J. C. Woicik, H. Park, J.-W. Kim, and P. J. Ryan, Phys. Rev. Lett. 120, 197201 (2018).
- ³⁶J. W. Freeland, J. Liu, M. Kareev, B. Gray, J. W. Kim, P. Ryan, R. Pentcheva, and J. Chakhalian, Europhys. Lett. 96, 57004 (2011).
- ³⁷Y. Song, X. Liu, F. Wen, M. Kareev, R. Zhang, Y. Pei, J. Bi, P. Shafer, A. T. N'Diaye, E. Arenholz, S. Y. Park, Y. Cao, and J. Chakhalian, *Phys. Rev. Mater.* 4, 024413 (2020).
- ³⁸H. L. Feng et al., J. Solid State Chem. **201**, 186 (2013).
- ³⁹G. Koster et al., Rev. Mod. Phys. **84**, 253 (2012).
- ⁴⁰T. L. Meyer, H. Jeen, X. Gao, J. R. Petrie, M. F. Chisholm, and H. N. Lee, Adv. Electron. Mater. 2, 1500201 (2016).
- ⁴¹ V. K. Wadhawan, Phase Transitions 3, 3 (1982).
- ⁴²J.-S. Zhou, J.-Q. Yan, and J. B. Goodenough, Phys. Rev. B **71**, 220103(R) (2005).
- ⁴³P. E. Vullum, R. Holmestad, H. L. Lein, J. Mastin, M.-A. Einarsrud, and T. Grande, Adv. Mater. **19**, 4399 (2007).
- ⁴⁴R. J. Green, M. W. Haverkort, and G. A. Sawatzky, Phys. Rev. B **94**, 195127 (2016).
- ⁴⁵ A. Subedi, O. E. Peil, and A. Georges, Phys. Rev. B **91**, 075128 (2015).
- ⁴⁶ A. Jana, S. Sahoo, S. Chowdhury, A. K. Mandal, S. Bimli, R. S. Devan, R. J. Choudhary, D. M. Phase, and A. K. Raychaudhuri, Phys. Rev. B 106, 205123 (2022).
- ⁴⁷P. C. Rogge et al., Phys. Rev. Mat. 2, 015002 (2018).
- ⁴⁸S. Sarkar, R. Raghunathan, S. Chowdhury, R. J. Choudhary, and D. M. Phase, Nano Lett. **21**, 8433 (2021).
- ⁴⁹S. Chowdhury, R. J. Choudhary, and D. M. Phase, ACS Appl. Electron. Mater. 3, 5095 (2021).
- ⁵⁰ A. Bagri, A. Jana, G. Panchal, S. Chowdhury, R. Raj, M. Kumar, M. Gupta, V. R. Reddy, D. M. Phase, and R. J. Choudhary, ACS Appl. Mater. Interfaces 15, 18391 (2023).
- ⁵¹S. Chowdhury, S. Majumder, R. Mishra, A. K. Mandal, A. Bagri, S. Yadav, S. Karmarkar, D. M. Phase, and R. J. Choudhary, arXiv:2308.04324 (2023).
- ⁵² M. Zheng, X.-K. Xu, H. Ni, Y.-P. Qi, X.-M. Li, and J. Gao, Appl. Phys. Lett. 112, 123502 (2018).
- ⁵³ M. Zheng, X. Y. Li, M. M. Yang, Q. X. Zhu, Y. Wang, X. M. Li, X. Shi, H. L. W. Chan, X. G. Li, H. S. Luo, and R. K. Zheng, Appl. Phys. Lett. **103**, 132910 (2013).